Journal of Natural Gas Science and Engineering 45 (2017) 575–583

Contents lists available at ScienceDirect

Journal of Natural Gas Science and Engineering

journal homepage: www.elsevier.com/locate/jngse

Effect of nano-confinement on high pressure methane flow characteristics

Zhehui Jin

School of Mining and Petroleum Engineering, Department of Civil and Environmental Engineering, University of Alberta, Edmonton, AB T6G 1H9, Canada

ARTICLE INFO

Article history:
Received 19 January 2017
Received in revised form
4 June 2017
Accepted 7 June 2017
Available online 24 June 2017

Keywords:
High pressure methane flow
Shale nanopore
Molecular simulation
Slip length

ABSTRACT

High pressure gas flow in shale nanoporous media plays an important role in shale gas recovery. The objective of this work is to study the effect of confinement on high pressure methane flow in nanoscale pores. We used dual control volume grand canonical molecular dynamics for different temperatures and pore sizes and compared our results with conventional hydrodynamic equation. We observed that when pore size is larger than 2 nm, flux increases with pore size. But when pore size is less than 2 nm, flux shows varying behaviors depending on the pore size due to methane molecular configurations and structures under different nano-confinements. We also observed that enhancement over the prediction from Hagen-Poiseuille equation can be more than two orders of magnitude in nanopores of around 1 nm pore size. Similar to previous computer simulation and experiments on liquid flow in nanopores, the dependences of the enhancement factor ε and the calculated slip length L_s on the pore sizes show discontinuity within three distinct regions: R1) pore size less than 0.8 nm; R2) between 0.8 and 1.0 nm; and R3) larger than 1.0 nm. Within R2 and R3, ε and L_s monotonically decrease with pore size. The methane molecular flux, enhancement factor, and calculated slip length increase from 328.15 K to 368.15 K, but remain comparable for 368.15 K and 408.15 K.

1. Introduction

Booming in shale gas industry in the past few years has stimulated profound interest in exploration and production activities. Fluid flow in shale media has a profound effect in shale gas recovery. Flow in conventional reservoirs is driven by pressure-driven convective flow, because pores and fractures are large. Continuum flow can be readily described by the Darcy law or classical Navier-Stoke (NS) equations (Travis et al., 1997; Firouzi and Wilcox, 2013; Neuman, 1977; Whitaker, 1986). In a continuum system, the behavior of a fluid can be described in terms of infinitesimal volumetric elements, which have well defined thermophysical properties. The application of Newton's second law to the system of volumetric elements leads to the NS equations (Thomas and McGaughey, 2009). However, shale has widely distributed nanopores in both organic and inorganic matters (Jin and Firoozabadi, 2016a; Li et al., 2014). The pore sizes in typical shale reservoirs can range from a few to hundreds of nanometers (Curtis et al., 2012; Loucks et al., 2009; Chalmers et al., 2012). Low pressure gas (N_2 and CO_2) adsorption analysis has shown that there are significant amount of pores with sub-2 nm diameter (Chalmers et al., 2012). In small nanopores, size of fluid molecule is comparable to the flow domain (Thomas and McGaughey, 2009) and molecular distribution is inhomogeneous (Li et al., 2014; Jin and Firoozabadi, 2015). In addition, strong surface adsorption can significantly increase the gas-in-place. The transport properties of fluids in such small nanopores deviate significantly from the conventional reservoirs (Jin and Firoozabadi, 2016a). As a result, the Darcy law and NS equations break down (Bitsanis et al., 1988).

Flow in nanopores can be classified into different flow regimes (Kandlikar et al., 2005). The Knudsen number Kn is the key parameter to categorize gas flow rarefaction, which is defined as the ratio of mean free path of fluid molecules λ to a characteristic dimension such as pore width W ($Kn = \lambda/W$) (Roohi and Darbandi, 2009). The mean free path of a molecule λ is given by (Jin and Firoozabadi, 2015)

E-mail address: zhehui2@ualberta.ca.

http://dx.doi.org/10.1016/j.jngse.2017.06.007
1875-5100/

$$\lambda = \frac{R_g T}{\sqrt{2}\pi\sigma^2 N_A P}, \quad (1)$$

in which R_g is the gas constant, T is temperature, σ is molecule diameter, N_A is the Avogadro number and P is pressure. For a given pore size, temperature and fluid, Kn is only dependent on pressure. If Knudsen number is sufficiently small, i.e., $Kn < 0.01$, the fluid flow can be assumed as continuum and the hydrodynamic Hagen-Poiseuille (HP) equations may describe flow with no-slip boundary conditions (Roohi and Darbandi, 2009). Assuming slit nanopores of width W, the HP equation for flux J^{HP} is given as

$$J^{HP} = -\frac{W^3}{12\eta}\left(\frac{\partial P}{\partial x}\right), \quad (2)$$

where η is viscosity and x is flow direction. If $0.01 < Kn < 0.1$, the flow is considered to be in a slip flow regime (Roohi and Darbandi, 2009). When there is slippage at the pore walls, Klinkenberg correction (Klinkenberg, 1941) is often applied to the continuum based models, which enhances fluid flow in nanopores. Most authors use correction factors associated with the macroscopic transport to describe the slip effect. The so-called fluid slip can lead to higher apparent permeability for porous media (Fathi et al., 2012). The slip effect can also be incorporated into the HP equation by using a theoretical dimensionless coefficient (Javadpour, 2009). The continuum flow with slip effect is given as (Jin and Firoozabadi, 2015)

$$J^{HP} = -\frac{W^3}{12\eta}\left(\frac{\partial P}{\partial x}\right)\left(1 + \frac{6L_s}{W}\right), \quad (3)$$

where L_s is the slip length, which is the distance extrapolated into the surface to obtain vanishing velocity as assumed by no-slip boundary condition (Jin and Firoozabadi, 2015; Cottin-Bizonne et al., 2003). If $0.1 < Kn < 10$, the fluid flow is considered to be in the transition regime, where the continuum-based flow model fails (Roohi and Darbandi, 2009). In the transition flow regime, gas slippage and collision with pore wall play important roles in fluid flow (Javadpour, 2009). In shale subsurface formations, pressure is on the order of few hundred bar and the flow regimes are mainly slip and transition flows (Zhang et al., 2015).

There have been a number of experimental measurements and computer simulations on gas and liquid flows in nanopores. Majumder et al. (2005). measured water and hydrocarbon flows in 7 nm diameter carbon nanotubes and compared to the non-slip HP flows. They found that enhancement ratios can be three to five orders of magnitude. Although the enhancement ratios were not as high as Majumder et al. (2005), Holt et al. (2006). found that water flow enhancement ratios can be three orders of magnitude for pore diameters less than 2 nm and the calculated slip length is in the range of micrometers. Whitby et al. (2008). found that the flow of hydrocarbons in 44 nm diameter carbon nanopipes still can be one order of magnitude larger than HP flow. Qin et al. (2011). measured water flow in carbon nanotubes with pore diameters from 0.8 to 1.6 nm and observed that flow enhancement factor does not show a monotonic increase with decreasing tube diameters and there exists a discontinuous region located around 0.98–1.10 nm. To better understand the flow dynamics in smaller pore diameters, Thomas and McGaughey (2009) used molecular dynamics (MD) simulations to study the flow enhancement of water through carbon nanotubes of diameter from 0.83 nm to 1.66 nm. They observed that there is discontinuous transition in flow enhancement in the region of diameter around 1.25–1.39 nm when there is a water molecular structure change from stacked hexagons to bulk-like liquid. They claimed that such discontinuity indicates a transition from continuum to subcontinuum transport. In subcontinuum region, because the pore size is comparable to the size of fluid molecules, flow enhancement may not increase monotonically with decreasing flow area due to confinement-induced changes to the liquid structure. Yasuoka et al. (2015). used MD simulations to study liquid argon flow in carbon nanotubes with diameters in the range from 0.81 to 21.7 nm. They also observed the discontinuous transition in flow enhancement induced by the change of the structural arrangement of the fluid molecules. In addition, the calculated slip length does not show a monotonic increase with decreasing pore diameter. Recently, Kazemi and Borujeni studied flow of various gas molecules in organic nanoscale channels of different pore sizes by using dual control volume grand canonical molecular dynamics simulations (Kazemi and Takbiri-Borujeni, 2016a). Wang et al. (2016). studied the effect of temperature and pore size on the calculated slip length on the supercritical CO_2 and octane flow through organic nanopores with slit apertures ranging from 0.4 nm to 5.2 nm by using non-equilibrium molecular dynamics simulations. In their simulation, they applied a constant external force on fluid molecules to represent the pressure gradient. They did not observe the discontinuous transition in flow enhancement and slip length. Although a number of experimental and computer simulation works have been reported on liquid and low pressure gas flow, the effect of nano-confinement and discontinuous transition on the flow enhancement and slip length of high pressure gas flow is not well studied.

In two recent papers, we have used the dual control-volume-grand-canonical molecular dynamics (DCV-GCMD) simulation to study methane flow in carbon nanopores (Jin and Firoozabadi, 2015, 2016b). Two control volumes are implemented, which lead to the development of steady-state chemical potential and pressure difference and enable a direct measurement of flow (Heffelfinger and Swol, 1994). We observed that methane molecules form strong adsorption layers in nanopores and the velocity of adsorption layer in flow direction is non-zero. In this work, we use DCV-GCMD to study high pressure methane flow through carbon nanopores and the effect of nano-confinement on the flow enhancement and slip length. Shale is composed of organic and inorganic materials. Organic materials which are mainly kerogen have pores in nanometer range. Kerogen is hydrophobic and can be simulated by carbon materials (Li et al., 2014). For simplicity, we use a full atomistic structure of graphite layers formed by carbon atoms to simulate slit-like nanopores. Based on the low pressure nitrogen adsorption (Zhang et al., 2016; Labani et al., 2013), in addition to slit-like pores, it has been revealed that shale can have other shaped pores such as ink-bottle (de Boer and Lippens, 1964; Sing et al., 2008). Furthermore, kerogen can have hetero-atoms on the surface and the pore surface may be rough (Falk et al., 2015). The roughness of surface may affect fluid flow in nanopores (de Almeida and Miranda, 2016). However, the purpose of this work is to compare with the HP flow and study how the enhancement factor and the slip length changes with pore size. In HP flow, the surface roughness is not taken into account. Both methane molecule and carbon atom are modeled by single-site Lennard-Jones (LJ) particles explicitly considering the Van der Waals interactions. By incorporating these features, our DCV-GCMD is expected to provide the effects of nanopore size and temperature on the high pressure methane flow and dependences of the flow enhancement and slip length on the pore size.

The remainder of this paper is organized as following. In section 2, we introduce molecular simulation methods and define molecular models used in this work. In section 3, we investigate high pressure methane flows in carbon nanopores and the effect of nano-confinement on flow enhancement and slip length. In

section 4, we summarize key conclusions and discuss implications.

2. Simulation methods

2.1. Model

The simulation box consists of three regions as shown in Fig. 1. The **H**, **L** and **C** regions correspond to the high and low chemical potential control volumes, and carbon nanopores, respectively. The **H** region is placed at the left end and **L** region is placed at the right end of box. The **C** region is placed between the two control volumes. We place confining walls (in yz plane) at each end of simulation box in x direction. The fluid molecules interact with these walls via a LJ interaction as a function of the particle's x-component distance from the wall (Heffelfinger and Swol, 1994). Thus, we apply periodic boundary condition in y and z directions. The sizes of **H** and **L** regions in x direction are fixed at 10 nm to ensure that they reduce to the corresponding bulk conditions. The box size is $(20 + L_c)\text{nm} \times 4.92\text{nm} \times (1.675 + W)\text{nm}$ in x, y and z directions, respectively, where L_c is the length of nanopores in x direction and W is the pore width, which is the separation distance between the centers of carbon atoms on the two layers forming a slit pore. The width of nanopores in y direction is the same as box size (4.92 nm).

The carbon atoms are placed according to the structure of graphite layers (Wang et al., 2006a, 2006b) to construct the nanopores. We use three graphite layers to form one carbon sheet and two carbon sheets are used to set up slit-like pores. The separation distance between carbon atom centers of two graphite layers is $\Delta = 0.335$ nm. The distance between two adjacent carbon atoms in the same graphite layer is $L_{cc} = 0.142$ nm. Thomas and McGaughey (2009) argued that the positions and movements of fluid molecules in short nanopores (less than 10 nm) are correlated and the inlet and outlet are not independent. To avoid such correlation, they suggested the pore length of 75 or 150 nm. In this work, the nanopore length is given as $L_c = 959L_{cc} = 136.178$ nm. Carbon sheets are fixed throughout the simulation.

As in our previous works (Jin and Firoozabadi, 2015, 2016b), we use the TraPPE model (Martin and Siepmann, 1998) to simulate methane molecules. The interactions between methane and carbon atoms and between methane molecules are described by the pairwise-additive LJ 12–6 potentials,

$$u_{LJ}(r_{ij}) = 4\varepsilon_{ij}\left[\left(\frac{\sigma_{ij}}{r_{ij}}\right)^{12} - \left(\frac{\sigma_{ij}}{r_{ij}}\right)^{6}\right] \tag{4}$$

where r_{ij}, ε_{ij}, and σ_{ij} are the separation, LJ well depth, and LJ size, respectively. Unlike interactions σ_{ij} and ε_{ij} are computed using the standard Lorentz-Berthelot combining rules: $\sigma_{ij} = (\sigma_{ii} + \sigma_{jj})/2$ and $\varepsilon_{ij} = \sqrt{\varepsilon_{ii}\varepsilon_{jj}}$. The values of size parameter σ and energy parameter ε for methane molecules and carbon atom are listed in Table 1. All of the LJ interactions are truncated at a distance of 1.07 nm. The interaction between a methane molecule and the nanopore is obtained by summing over all carbon atoms in the nanopores.

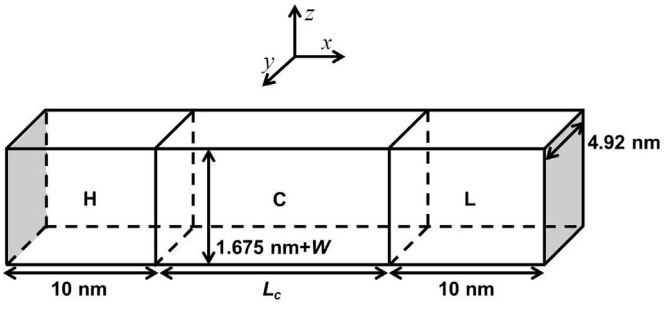

Fig. 1. Schematic representation of simulation box. The molecules flow along the $-x$ and $+x$ direction.

The methane-wall interaction is given by a 9-3 Lennard-Jones potential (Lupkowski and van Swol, 1990) at its minimum, $x_{\min} = 0.4^{1/6}\sigma_{sf}$,

$$V^{ext}(x) = \begin{cases} \varepsilon_{sf}\left[\frac{2}{15}\left(\frac{\sigma_{sf}}{x}\right)^9 - \left(\frac{\sigma_{sf}}{x}\right)^3\right], & x < x_{\min} \\ 0, & x \geq x_{\min} \end{cases}, \tag{5}$$

in which x is the distance from the methane molecule to the wall, σ_{sf} and ε_{sf} are obtained from the Lorentz-Berthelot combining rules of size and energy parameters of carbon and methane molecules. We note that the flow predictions from the 20-nm control volume are similar to 10-nm control volume. So the effect of repulsive wall with 10-nm control volume on the flow is negligible.

2.2. Dual control volume grand canonical molecular dynamics

DCV-GCMD method has been used to study chemical potential-driven flow through membranes (Wang et al., 2006a, 2006b) and slit nanopores (Firouzi and Wilcox, 2013; Jin and Firoozabadi, 2015; Kazemi and Takbiri-Borujeni, 2016a; Jin and Firoozabadi, 2016b; Cracknell et al., 1995; Kazemi and Takbiri-Borujeni, 2016b). It combines the MD moves in the entire system with the grand canonical Monte Carlo (GCMC) particle insertion and deletion of molecules in the two control volumes (CVs). In our work, MD and GCMC moves are only applied to methane molecules.

Throughout the simulation volume, a standard MD simulation moves are employed. The equations of motion are solved by the Verlet velocity algorithm (Swope et al., 1982) using the Berendsen thermostat (Berendsen et al., 1984) to maintain constant temperature. Linked cells (Allen and Tildesley, 1987) are employed to reduce the computation time. The chemical potentials of methane in the CVs are maintained using a sufficient number of GCMC insertion and deletion (Heffelfinger and Swol, 1994; Ford and Heffelfinger, 1998; Xu et al., 1998). The probability of inserting an methane molecule p^+ is given by

$$p^+ = \min\left\{\frac{ZV_{CV}}{N_{CV}+1}\exp\left(-\frac{\Delta U}{k_BT}\right), 1\right\} \tag{6}$$

where $Z = \exp(\mu/k_BT)/\Lambda^3$ is the absolute activity at temperature T, Λ is the de Broglie wavelength, μ is the chemical potential, k_B is the Boltzmann's constant, ΔU is the potential energy change resulting from inserting or removing a molecule, V_{CV} is the volume of CV and N_{CV} is the number of methane molecules in each CV. As the particles are created, they are given velocities satisfying the Maxwell-Boltzmann distribution (Papadopoulou et al., 1993). The probability of deleting a molecule p^- is given by

$$p^- = \min\left\{\frac{N_{CV}}{ZV_{CV}}\exp\left(-\frac{\Delta U}{k_BT}\right), 1\right\}. \tag{7}$$

Table 1
LJ parameters used in the simulations.

Molecules	σ (nm)	ε/kB (K)	Reference
CH_4	0.373	148.0	(Martin and Siepmann, 1998)
C	0.34	28.0	(Steele, 1973)

100 GCMC moves in each CV are followed by one MD integration step. The chemical potentials are obtained from Widom's particle insertion method (Widom, 1963) in *NVT* Monte Carlo simulations of bulk fluids. The time step of MD simulation is $\Delta t = 2$ fs. We use 10-ns simulation time for system to reach steady state and 20-ns simulation time to calculate density, velocity profiles and fluxes.

The flux of methane molecules J^x is obtained by counting the net number of particles crossing halfway along nanopore region (Heffelfinger and Swol, 1994; Vieira-Linhares and Seaton, 2003):

$$J^x = \frac{n^{hl} - n^{lh}}{n_t \Delta t A_{yz}}, \tag{8}$$

where n^{hl} and n^{lh} are the number of molecules moving from high to low pressure region and vice versa, n_t is the number of time step of sampling, A_{yz} is the cross-section area of carbon nanopore.

3. Results and discussions

In this section, we present the flux, flow enhancement, and calculated slip length of high pressure methane flow of different pore sizes in carbon nanopores. We study methane flow between control volumes at pressures $P_h = 300$ bar and $P_l = 280$ bar and various temperatures. We will explicitly investigate the effect of pore sizes and temperatures.

3.1. Methane molecular flux in nanopores

In Fig. 2, we present the methane molecular fluxes with various pore sizes and temperatures through carbon nanopores. Overall, as pore size increases, molecular flux increases. However, there is discontinuity around $W = 1.0$ nm: flux decreases from 0.9 to 1.0 nm pores, then increases from 1.0 to 1.1 nm. In addition, there is big jump in flux from 0.7 to 0.8 nm pores. These behaviors (when pore size is less than 1.0 nm) may be due to the changes in molecular configurations and structures under nano-confinement, which we will discuss later. For $T = 328.15$ K, flux increases with pore size for $W \geq 1.1$ nm. But for higher temperatures ($T = 368.15$ and 408.15 K), flux is generally constant from 1.1 to 2.0 nm pores. When $W \geq 2.0$ nm, flux increases with pore size for all temperature conditions. A slight increase in flux is overserved from 328.15 K to 368.15 K, especially for pores less than 2 nm. Such increase may be attributed to the higher kinetic energy due to higher temperature. However, flux becomes comparable for 368.15 K and 408.15 K. The effect of temperature on confined methane flow agrees well with supercritical CO_2 flow in organic nanopores in shale (Wang et al., 2016).

To study the effect of pore size on methane flow, we present the methane density distributions in the middle of the pores with W from 0.7 to 5.0 nm for $T = 368.15$ K in Fig. 3. Similar to our previous works (Jin and Firoozabadi, 2015, 2016b), at high pressures, methane density profiles in nanopores are similar at different positions of the pores. As a result, we only present the density profiles in the middle of the pores. For $W = 0.7$ nm, because the pore space is small, the adsorption layers on each side of surfaces overlap and methane forms only one strong adsorption layer in the middle the pores. For $W = 0.8$ nm, the adsorption layers still overlap, but the strength is greatly reduced. When $W \geq 0.9$ nm, methane can form adsorption layer on each side of surface. However, the peak of surface adsorption layer has a non-monotonic behavior as pore size

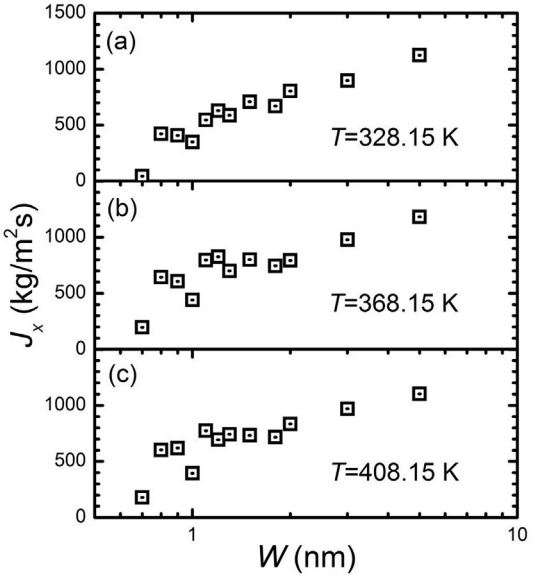

Fig. 2. Methane molecular fluxes from DCV-GCMD between control volume pressure $P_h = 300$ bar and $P_l = 280$ bar for the various nanopore sizes and temperatures.

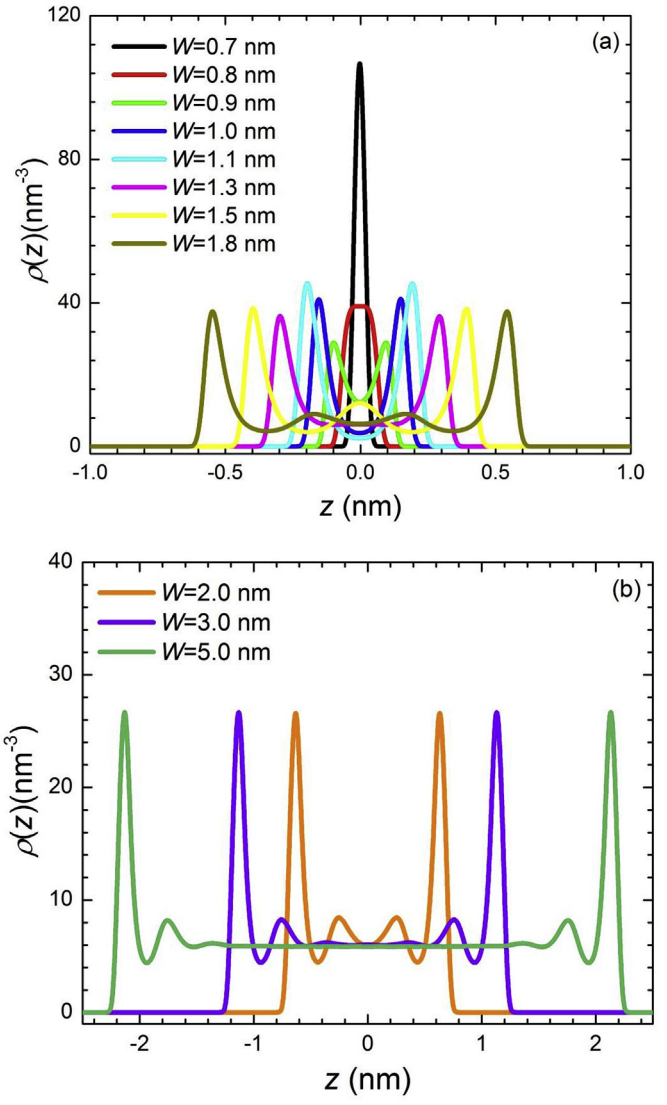

Fig. 3. Methane density distribution in the middle the pores at $T = 368.15$ K for pore sizes (a) from 0.7 to 1.8 nm; (b) from 2.0 to 5.0 nm.

increases. From 0.9 to 1.1 nm pores, it increases with pore size and reaches peak at 1.1 nm pores. Then, it decreases for 1.3 nm pores and increases again for 1.5 nm pores. After 1.5 nm pores, the peak of surface adsorption layer decreases with pore size and reaches a plateau. For 1.5 nm pores, the second weak adsorption layers on each side of surface overlap. As a result, methane molecules can have a weak second adsorption layer in the middle of the pores. When $W \geq 1.8$ nm, methane forms a weak second adsorption layer on each side of surfaces. The non-monotonic behavior with pore size also can be seen in the average methane densities ρ_{ave} in the nanopores as shown in Fig. 4, which is obtained by

$$\rho_{ave} = \frac{\langle N_c \rangle}{V_c}, \tag{9}$$

where $\langle N_c \rangle$ is the ensemble average number of molecules in the nanopores and $V_c = L_c \times 4.92 \times W$ nm^3 is the pore volume. The non-monotonic behavior in ρ_{ave} agrees well with the trend of peak of surface adsorption layer for $W \leq 1.5$ nm. When $W \geq 1.5$ nm, as the contribution of surface adsorption layer to average methane density decreases with pore size, ρ_{ave} decreases with pore size.

Flux is not only dependent on the density distributions, but also on the molecular velocity distributions. We present the methane molecular velocity distributions in the middle of the pores with W from 0.7 to 5.0 nm for $T = 368.15$ K in Fig. 5. There are some fluctuations in the velocity distributions, especially in the middle of the pores. It is mainly because there are fewer methane molecules in the middle of the pores than that on the surfaces as shown in Fig. 4, resulting in the smaller sample size for velocity distribution calculation. Such fluctuation was also seen in our previous work (Jin and Firoozabadi, 2015) and the work by Kazemi and Borujeni (Kazemi and Takbiri-Borujeni, 2016a). When $W = 0.7$ nm, velocity profile has parabolic behavior; coupling with density distributions shown in Fig. 3(a), methane molecules can only flow through the single-layered structure in such small nanopores. Because the confined methane molecules are highly packed, the velocity distribution is greatly reduced. When pore size is larger than 0.7 nm, the velocity distributions have non-parabolic behavior which agrees well with our previous works (Jin and Firoozabadi, 2015, 2016b). Molecular velocity on the surface is comparable to the middle of the pores. Similar to the density distribution, the velocity distribution has non-monotonic behavior; it increases with pore size from 0.7 to 0.9 nm, then decreases for 1.0 nm pores. Such decrease is the main reason why flux has discontinuous behavior around $W = 1.0$ nm, which is also seen in the enhancement factor over HP equation as we will discuss later. When $W \geq 1.0$ nm, the velocity distribution increases with pore size. For $W = 5.0$ nm, molecular velocity in the middle of the pores is slightly higher than that on the surface. Due to non-monotonic behavior in ρ_{ave} from 1.0 to 2.0 nm pores, the molecular fluxes in this region become comparable. When $W \geq 2.0$ nm, flux increase with pore size is mainly because velocity distribution increases with pore size.

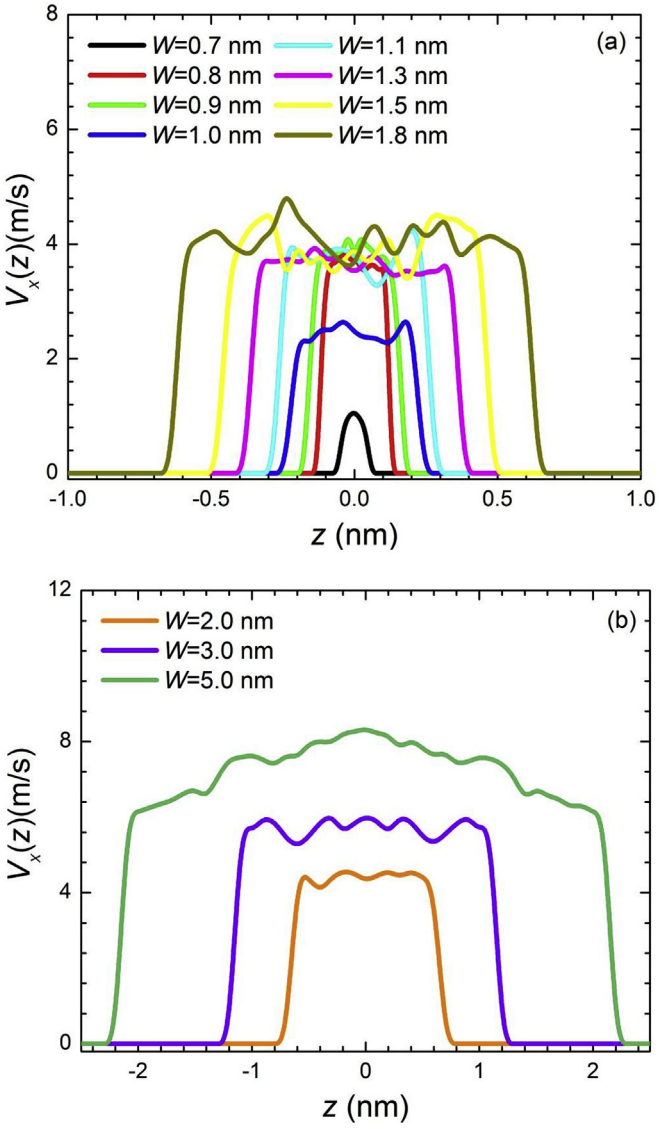

Fig. 5. Methane molecular velocity distributions in the middle the pores at $T = 368.15$ K for pore sizes (a) from 0.7 to 1.8 nm; (b) from 2.0 to 5.0 nm.

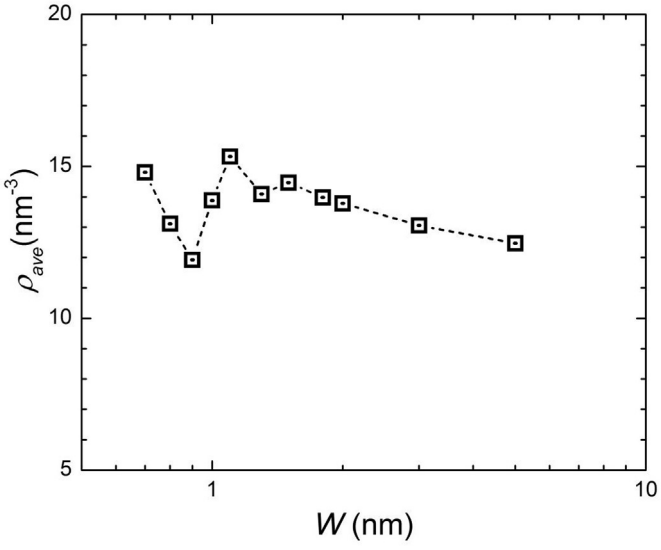

Fig. 4. Average methane densities in the nanopores at $T = 368.15$ K.

To understand the effect of temperature on the flux, we first present the methane density distributions with different pore sizes and at three different temperature conditions in Fig. 6. It can be seen that the overall shape of methane density distribution does not change with temperature. For 0.9 nm and 1.0 nm pores, methane can only form one strong adsorption layer on each pore surface wall; for 1.5 nm pores, methane can form one weak adsorption layer in the middle of the pore; for 3.0 nm pores, methane forms a weak second adsorption layer. As temperature increases, the methane molecular distribution decreases. Opposite

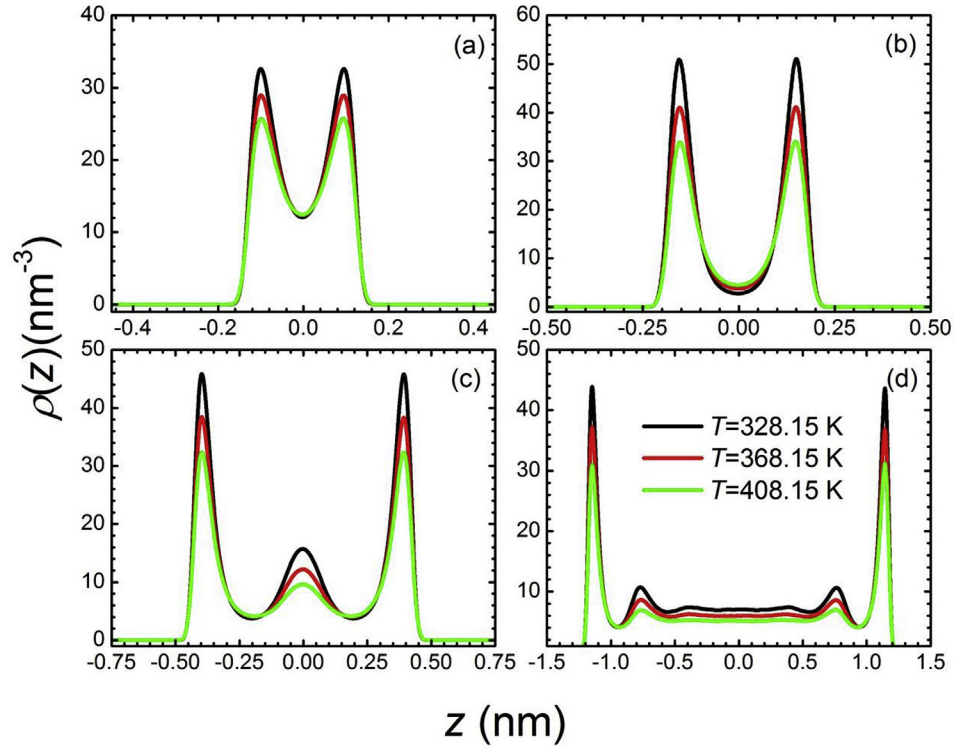

Fig. 6. Methane density distribution in the middle the pores at 328.15 K, 368.15 K, and 408.15 K for pore sizes (a) 0.9 nm; (b) 1.0 nm; (c) 1.5 nm; (d) 3.0 nm.

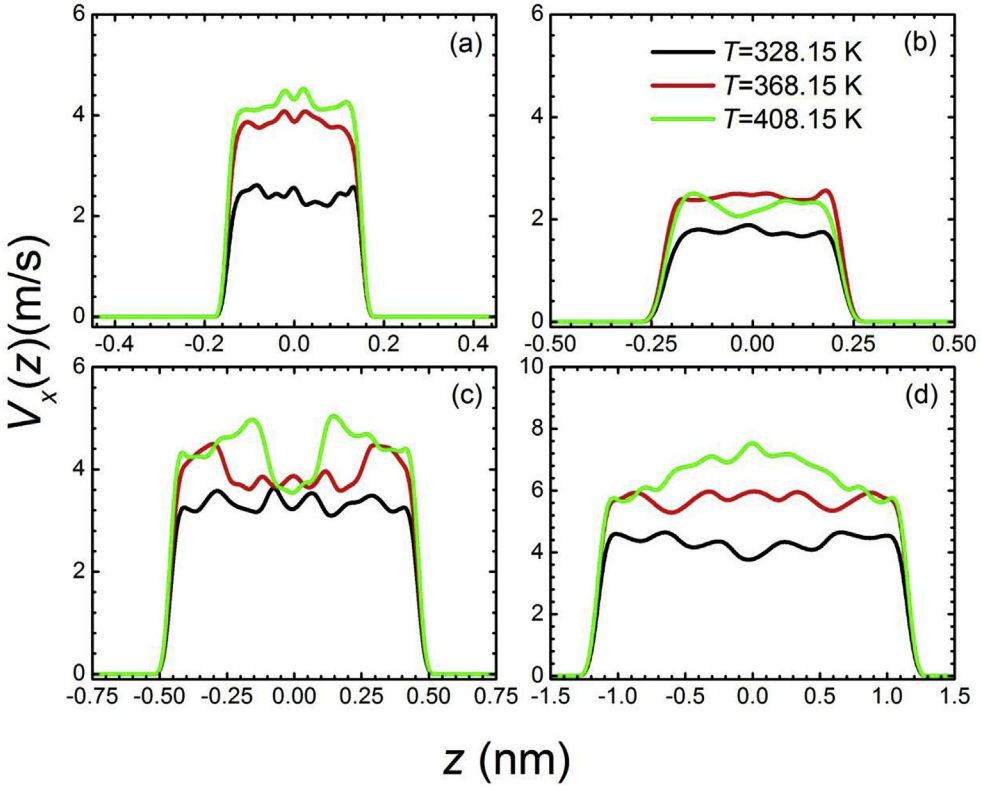

Fig. 7. Methane velocity distribution in the middle the pores at 328.15 K, 368.15 K, and 408.15 K for pore sizes (a) 0.9 nm; (b) 1.0 nm; (c) 1.5 nm; (d) 3.0 nm.

behavior can be seen from the methane molecular velocity distributions as shown in Fig. 7. Generally, as temperature increases, molecular velocity distribution increases. For 0.9 nm and 1.0 nm pores, molecular velocity on the wall is similar to that in the middle of the pores. However, for all temperature conditions, as pore size increases from 0.9 nm to 1.0 nm, the velocity distribution decreases.

Although the density distribution increases from 0.9 nm to 1.0 nm as shown in Fig. 6, the decrease in velocity distributions causes the sudden drop in the methane fluxes. Such decrease in methane molecular flux is probably due to the molecular configurations and structures in nanopores. For 1.5 nm pores, as temperature increases, the methane molecular velocity in the middle of the pores becomes lower than that on the surfaces. The lower molecular velocity in the middle of the pores is due to the accumulation of methane molecules. For 3.0 nm pores, opposite behavior is observed; as temperature increases, the methane molecular velocity in the middle of the pores is higher than that on the surfaces in line with our previous work (Jin and Firoozabadi, 2015).

In the following subsections, we investigate the enhancement factor over HP equation and slip length.

3.2. Enhancement over HP equation

As shown in Fig. 8, the discontinuity in the methane molecular fluxes results in the discontinuity in enhancement factor ε over HP equation, which is given by

$$\varepsilon = \frac{J^x}{J^{HP}}. \tag{10}$$

Assuming linear pressure dependence between the inlet and outlet in the HP expression in Eq. (2), Eq. (10) can be simplified as

$$\varepsilon = \frac{J^x}{J^{HP}} = \frac{12\eta L_c J^x}{W^3(P_h - P_l)}. \tag{11}$$

We use the mean viscosity of bulk fluids at P_h and P_l. The data are from the National Institute of Standards and Technology (NIST) Chemistry WebBook. ε can be divided into three different regions: R1) pore size less than 0.8 nm; R2) between 0.8 and 1.0 nm; and R3) larger than 1.0 nm. As shown in Eq. (2), HP equation predicts that flux monotonically increases with pore size; but methane molecular flux has a non-monotonic behavior as shown in Fig. 3. When pore size is less than 0.8 nm, methane can only form single-layered structure and velocity distributions are greatly reduced. As a result, the enhancement over HP equation is small. As pore size increases, the first transition takes place as single-layered density distributions decrease and adsorption layer forms on each pore surfaces. In Region R2, ε decreases with pore size. For 0.8 nm pores, the enhancement can be as much as two orders of magnitude for 368.15 K and 408.15 K. The second discontinuity in ε occurs around 1.0 nm pores in line with molecular simulations and experimental measurement on water (Thomas and McGaughey, 2009; Qin et al., 2011) and liquid argon (Yasuoka et al., 2015) flow in carbon nanotubes. As shown in Fig. 3, when pore size is 1 nm, the separation between the peak points in the two adsorption layers on each pore surfaces is around 0.3 nm, which is less than the methane molecule size (LJ diameter of 0.373 nm). As a result, these two adsorption layers may be correlated. While pore size is larger than 1 nm, the separation distance is larger than the methane molecule size and the correlation effect becomes less significant. Methane molecules are predominantly adsorbed on the pore surfaces and the mobility of adsorption layers plays a key role in flow in nanopores (Jin and Firoozabadi, 2015). In Region R3, ε monotonically decreases with pore size. We also modeled low pressure methane flow between $P_h = 3$ bar and $P_l = 1$ bar and compared with Knudsen diffusion, which is considered to be valid for low pressure flow (Jin and Firoozabadi, 2015). We did not observe discontinuity in enhancement factor over Knudsen diffusion (not shown here). The enhancement factor increases from 328.15 K to 368.15 K, but becomes comparable for 368.15 K and 408.15 K. As pore size increases, the enhancement factor becomes comparable for all temperature conditions (e.g., $W = 5.0$ nm).

3.3. Discontinuity in calculated slip length

We calculate the effective slip length L_s by matching the actual methane flow J^x to Eq. (3),

$$L_s = -\frac{W}{6}\left(\frac{J^x \cdot 12\eta}{W^3}\frac{dx}{dP} - 1\right). \tag{12}$$

Again, assuming linear pressure dependence between the inlet and outlet and using the relation given in Eq. (11), Eq. (12) can be simplified as

$$L_s = \frac{W}{6}\left(\frac{J^x \cdot 12\eta}{W^3}\frac{L_c}{P_h - P_l} - 1\right) = \frac{W}{6}(\varepsilon - 1). \tag{13}$$

We present the calculated L_s in Fig. 9. The same as the enhancement factor ε, there is discontinuity in the calculated L_s with three different regions: R1, R2, and R3. Within R2 and R3, L_s

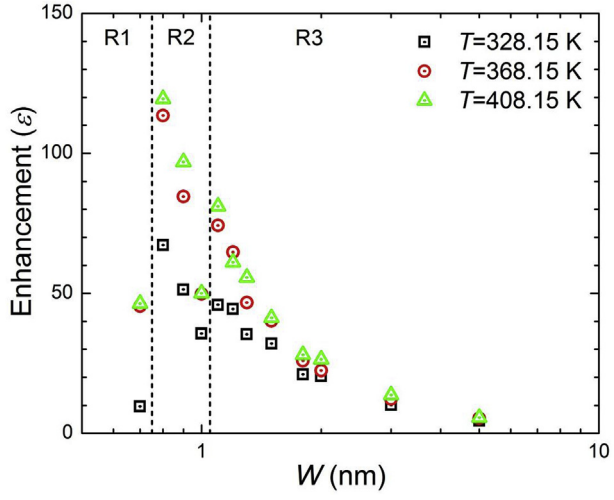

Fig. 8. The enhancement factor ε over HP equation of high pressure methane flow for pore sizes from 0.7 to 5.0 nm. The dashed lines are used to highlight the three different regions.

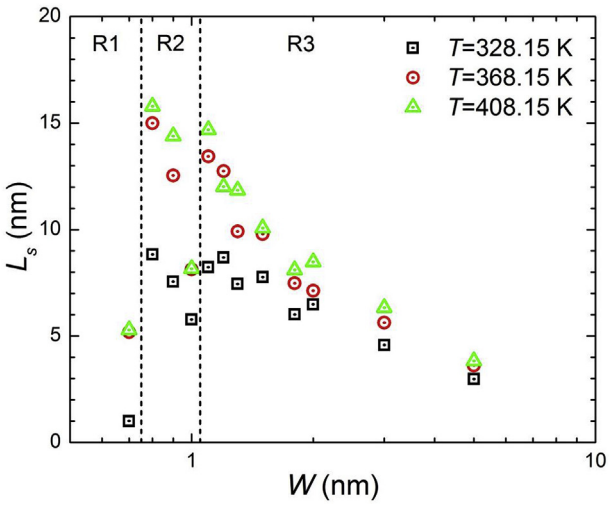

Fig. 9. Calculated slip length L_s of high pressure methane flow for pore sizes from 0.7 to 5.0 nm. The dashed lines are used to highlight the three different regions.

decreases with pore sizes for all temperature conditions as shown in Fig. 9. As a result, the largest calculated L_s is around 16 nm, when the pore size is close to 0.8 nm. L_s increases from 328.15 K to 368.15 K for all of pore sizes, but becomes comparable for 368.15 K and 408.15 K. Wang et al. (2016). found that with increasing temperature, the slip length increases and when $T > 390$ K, starts to converge to a constant.

4. Conclusions

In this work, we used DCV-GCMD simulations to study high pressure methane flow in nanopores at different temperature conditions and varying pore sizes. We also compared our results with hydrodynamic equation predictions and calculated the enhancement factor over HP equation as well as slip length.

We found that methane molecular flux has non-monotonic behavior with pore size when $W < 2$ nm; When $W \geq 2$ nm, flux increases with pore size. Methane molecular density distribution decreases with temperature, but velocity distribution increases. As a result, the flux increases as temperature increases from 328.15 K to 368.15 K, but becomes comparable for 368.15 K and 408.15 K. In other words, the decrease in density distributions is compensated by the higher velocity distributions, as temperature increases. Both of the enhancement factor ε over HP equation and the calculated slip length L_s show discontinuity in line with previous computer simulations and experiments on water (Thomas and McGaughey, 2009; Qin et al., 2011) and liquid argon (Yasuoka et al., 2015) flow. ε and L_s have three distinct regions. Within R2 and R3, ε and L_s monotonically decrease with pore size. But they have a sudden jump from 1.0 nm to 1.1 nm. ε and L_s increase as temperature increases from 328.15 K to 368.15 K, but become comparable for 368.15 K and 408.15 K. The enhancement over HP equation can be as much as two orders of magnitude. The HP equation ignores surface adsorption and assumes that velocity on the surface is zero.

This work should provide some insights into gas flow in shale nanoporous media as well as nanofluidics. In the future, we plan to investigate the effect of pressure on the gas flow in nanopores as well as enhancement over hydrodynamic equations.

Acknowledgement

This research was enabled in part by support provided by Westgrid (www.westgrid.ca) and Compute Canada (www.computecanada.ca). This research is financially supported by the Discovery Grant by Natural Sciences and Engineering Research Council of Canada (NSERC RGPIN-2017-05080).

References

Allen, M.P., Tildesley, D.J., 1987. Computer Simulation of Liquids. Clarendon, Oxford.
Berendsen, H.J.C., Postma, J.P.M., van Gunsteren, W.F., DiNola, A., Haak, J.R., 1984. Molecular dynamics with coupling to an external bath. J. Chem. Phys. 81 (8), 3684–3690.
Bitsanis, I., Vanderlick, T.K., Tirrell, M., Davis, H.T., 1988. A tractable molecular theory of flow in strongly inhomogeneous fluids. J. Chem. Phys. 89 (5), 3152–3162.
Chalmers, G.R., Bustin, R.M., Power, I.M., 2012. Characterization of gas shale pore systems by porosimetry, pycnometry, surface area, and field emission scanning electron microscopy/transmission electron microscopy image analyses: examples from the Barnett, Woodford, Haynesville, Marcellus, and Doig units. AAPG Bull. 96 (6), 1099–1119.
Cottin-Bizonne, C., Barrat, J.-L., Bocquet, L., Charlaix, E., 2003. Low-friction flows of liquid at nanopatterned interfaces. Nat. Mater 2 (4), 237–240.
Cracknell, R.F., Nicholson, D., Quirke, N., 1995. Direct molecular dynamics simulation of flow down a chemical potential gradient in a slit-shaped micropore. Phys. Rev. Lett. 74 (13), 2463.
Curtis, M.E., Sondergeld, C.H., Ambrose, R.J., Rai, C.S., 2012. Microstructural investigation of gas shales in two and three dimensions using nanometer-scale resolution imaging. AAPG Bull. 96 (4), 665–677.
de Almeida, J.M., Miranda, C.R., 2016. Improved oil recovery in nanopores: NanoIOR. Sci. Rep. 6, 28128.
de Boer, J.H., Lippens, B.C., 1964. Studies on pore systems in catalysts II. The shapes of pores in aluminum oxide systems. J. Catal. 3 (1), 38–43.
Falk, K., Coasne, B., Pellenq, R., Ulm, F.-J., Bocquet, L., 2015. Subcontinuum mass transport of condensed hydrocarbons in nanoporous media. Nat. Commun. 6.
Fathi, E., Tinni, A., Akkutlu, I.Y., 2012. Correction to Klinkenberg slip theory for gas flow in nano-capillaries. Int. J. Coal Geol. 103 (0), 51–59.
Firouzi, M., Wilcox, J., 2013. Slippage and viscosity predictions in carbon micropores and their influence on CO2 and CH4 transport. J. Chem. Phys. 138 (6), 064705.
Ford, D.M., Heffelfinger, G.S., 1998. Massively parallel dual control volume grand canonical molecular dynamics with LADERA II. Gradient driven diffusion through polymers. Mol. Phys. 94 (4), 673–683.
Heffelfinger, G.S., Swol, F.v., 1994. Diffusion in Lennard-Jones fluids using dual control volume grand canonical molecular dynamics simulation (DCV-GCMD). J. Chem. Phys. 100 (10), 7548–7552.
Holt, J.K., Park, H.G., Wang, Y., Stadermann, M., Artyukhin, A.B., Grigoropoulos, C.P., Noy, A., Bakajin, O., 2006. Fast mass transport through sub-2-nanometer carbon nanotubes. Science 312 (5776), 1034–1037.
Javadpour, F., 2009. Nanopores and apparent permeability of gas flow in mudrocks (shales and siltstone). J. Can. Petroleum Technol. 48 (8), 16–21.
Jin, Z., Firoozabadi, A., 2015. Flow of methane in shale nanopores at low and high pressure by molecular dynamics simulations. J. Chem. Phys. 143 (10), 104315.
Jin, Z., Firoozabadi, A., 2016. Thermodynamic modeling of phase behavior in shale media. SPE J. 21 (01), 190–207.
Jin, Z., Firoozabadi, A., 2016. Phase behavior and flow in shale nanopores from molecular simulations. Fluid Phase Equilibria 430, 156–168.
Kandlikar, S., Garimella, S., Li, D., Colin, S., King, M.R., 2005. Heat Transfer and Fluid Flow in Minichannels and Microchannels. Elsevier, London.
Kazemi, M., Takbiri-Borujeni, A., 2016. Flow of gases in organic nanoscale channels: a boundary-driven molecular simulation study. Energy & Fuels 30 (10), 8156–8163.
Kazemi, M., Takbiri-Borujeni, A., 2016. Non-equilibrium molecular dynamics simulation of gas flow in organic nanochannels. J. Nat. Gas Sci. Eng. 33, 1087–1094.
Klinkenberg, L.J., 1941. The Permeability of Porous Media to Liquids and Gases, in Drilling and Production Practice. American Petroleum Institute.
Labani, M.M., Rezaee, R., Saeedi, A., Hinai, A.A., 2013. Evaluation of pore size spectrum of gas shale reservoirs using low pressure nitrogen adsorption, gas expansion and mercury porosimetry: a case study from the Perth and Canning Basins, Western Australia. J. Petroleum Sci. Eng. 112, 7–16.
Li, Z., Jin, Z., Firoozabadi, A., 2014. Phase behavior and adsorption of pure substances and mixtures and characterization in nanopore structures by density functional theory. SPE J. 19 (06), 1096–1109.
Loucks, R.G., Reed, R.M., Ruppel, S.C., Jarvie, D.M., 2009. Morphology, genesis, and distribution of nanometer-scale pores in siliceous mudstones of the Mississippian Barnett Shale. J. Sediment. Res. 79 (12), 848–861.
Lupkowski, M., van Swol, F., 1990. Computer simulation of fluids interacting with fluctuating walls. J. Chem. Phys. 93 (1), 737–745.
Majumder, M., Chopra, N., Andrews, R., Hinds, B.J., 2005. Nanoscale hydrodynamics: enhanced flow in carbon nanotubes. Nature 438 (7064), 44, 44.
Martin, M.G., Siepmann, J.I., 1998. Transferable potentials for phase equilibria. 1. United-atom description of n-alkanes. J. Phys. Chem. B 102 (14), 2569–2577.
Neuman, S.P., 1977. Theoretical derivation of Darcy's law. Acta Mech. 25 (3–4), 153–170.
Papadopoulou, A., Becker, E.D., Lupkowski, M., van Swol, F., 1993. Molecular dynamics and Monte Carlo simulations in the grand canonical ensemble: local versus global control. J. Chem. Phys. 98 (6), 4897–4908.
Qin, X., Yuan, Q., Zhao, Y., Xie, S., Liu, Z., 2011. Measurement of the rate of water translocation through carbon nanotubes. Nano Lett. 11 (5), 2173–2177.
Roohi, E., Darbandi, M., 2009. Extending the Navier–Stokes solutions to transition regime in two-dimensional micro- and nanochannel flows using information preservation scheme. Phys. Fluids 21 (8), 082001 (1994-present).
Sing, K.S.W., Everett, D.H., Haul, R.A.W., Moscou, L., Pierotti, R.A., Rouquerol, J., Siemieniewska, T., 2008. Reporting physisorption data for gas/solid systems. In: Handbook of Heterogeneous Catalysis. Wiley-VCH Verlag GmbH & Co. KGaA.
Steele, W.A., 1973. The physical interaction of gases with crystalline solids: I. Gas-solid energies and properties of isolated adsorbed atoms. Surf. Sci. 36 (1), 317–352.
Swope, W.C., Andersen, H.C., Berens, P.H., Wilson, K.R., 1982. A computer simulation method for the calculation of equilibrium constants for the formation of physical clusters of molecules: application to small water clusters. J. Chem. Phys. 76 (1), 637–649.
Thomas, J.A., McGaughey, A.J.H., 2009. Water flow in carbon nanotubes: transition to subcontinuum transport. Phys. Rev. Lett. 102 (18), 184502.
Travis, K.P., Todd, B.D., Evans, D.J., 1997. Departure from Navier-Stokes hydrodynamics in confined liquids. Phys. Rev. E 55 (4), 4288–4295.
Vieira-Linhares, A., Seaton, N., 2003. Non-equilibrium molecular dynamics simulation of gas separation in a microporous carbon membrane. Chem. Eng. Sci. 58 (18), 4129–4136.
Wang, S., Yu, Y., Gao, G., 2006. Non-equilibrium molecular dynamics simulation on pure gas permeability through carbon membranes. Chin. J. Chem. Eng. 14 (2), 164–170.
Wang, S.-M., Yu, Y.-X., Gao, G.-H., 2006. Grand canonical Monte Carlo and non-equilibrium molecular dynamics simulation study on the selective adsorption and fluxes of oxygen/nitrogen gas mixtures through carbon membranes. J. Membr. Sci. 271 (1–2), 140–150.

Wang, S., Javadpour, F., Feng, Q., 2016. Fast mass transport of oil and supercritical carbon dioxide through organic nanopores in shale. Fuel 181, 741–758.
Whitaker, S., 1986. Flow in porous media I: a theoretical derivation of Darcy's law. Transp. Porous Media 1 (1), 3–25.
Whitby, M., Cagnon, L., Thanou, M., Quirke, N., 2008. Enhanced fluid flow through nanoscale carbon pipes. Nano Lett. 8 (9), 2632–2637.
Widom, B., 1963. Some topics in the theory of fluids. J. Chem. Phys. 39 (11), 2808–2812.
Xu, L., Sedigh, M.G., Sahimi, M., Tsotsis, T.T., 1998. Nonequilibrium molecular dynamics simulation of transport of gas mixtures in nanopores. Phys. Rev. Lett. 80 (16), 3511.
Yasuoka, H., Takahama, R., Kaneda, M., Suga, K., 2015. Confinement effects on liquid-flow characteristics in carbon nanotubes. Phys. Rev. E 92 (6), 063001.
Zhang, P., Hu, L., Meegoda, J.N., Gao, S., 2015. Micro/Nano-pore network analysis of gas flow in shale matrix. Sci. Rep. 5, 13501.
Zhang, Y., Shao, D., Yan, J., Jia, X., Li, Y., Yu, P., Zhang, T., 2016. The pore size distribution and its relationship with shale gas capacity in organic-rich mudstone of Wufeng-Longmaxi Formations, Sichuan Basin, China. J. Nat. Gas Geoscience 1 (3), 213–220.